

See discussions, stats, and author profiles for this publication at:
<https://www.researchgate.net/publication/226150769>

Ca²⁺ Imaging: Principles of Analysis and Enhancement

CHAPTER *in* NEUROMETHODS · FEBRUARY 2009

DOI: 10.1007/978-1-60761-476-0_3

CITATIONS

4

READS

43

2 AUTHORS:



Fabio Mammano

CNR

90 PUBLICATIONS 2,308 CITATIONS

SEE PROFILE



Mario Bortolozzi

Venetian Institute of Molecular Me...

31 PUBLICATIONS 602 CITATIONS

SEE PROFILE

Chapter 3

Ca²⁺ Imaging: Principles of Analysis and Enhancement

Fabio Mammano and Mario Bortolozzi

Abstract

In this chapter, we review the theoretical and experimental foundations underling a quantitative approach to Ca²⁺ imaging, discuss equilibrium conditions and their violations and present a computational framework that can be used to estimate the spatial and temporal dynamics of Ca²⁺ signals based of fluorescence measurements with Ca²⁺ indicators.

Key words: Buffers, Law of mass action, Binding reactions, Fluorescent indicators, Optical measurement of Ca²⁺ concentration, Single wavelength and ratiometric imaging, Chemical equilibrium, Non-equilibrium conditions, Diffusion, Ion fluxes, Differential equations, Monte Carlo methods

1. Optical Measurement of Ca²⁺ Concentration

Optical measurement of the intracellular concentration of selected ion species is paramount to understanding cell physiology and function. Several molecular probes, namely fluorescent dyes, capable of sensing the local ion concentration with high selectivity have been developed over the last 20 years. These are based on BAPTA (1,2-bis(o-aminophenoxy)ethane-*N,N,N',N'*-tetraacetic acid), a pH-insensitive evolution of the widely used Ca²⁺-selective chelator EGTA (ethylene glycol tetraacetic acid) (Fig. 3.1). Chelation is the binding or complexation of a bi- or multidentate ligand with a single metal ion. The mechanism of Ca²⁺ chelation by BAPTA is shown in Fig. 3.2.

Chelation of Ca²⁺ by a buffer B to form a complex CaB is described by the reaction

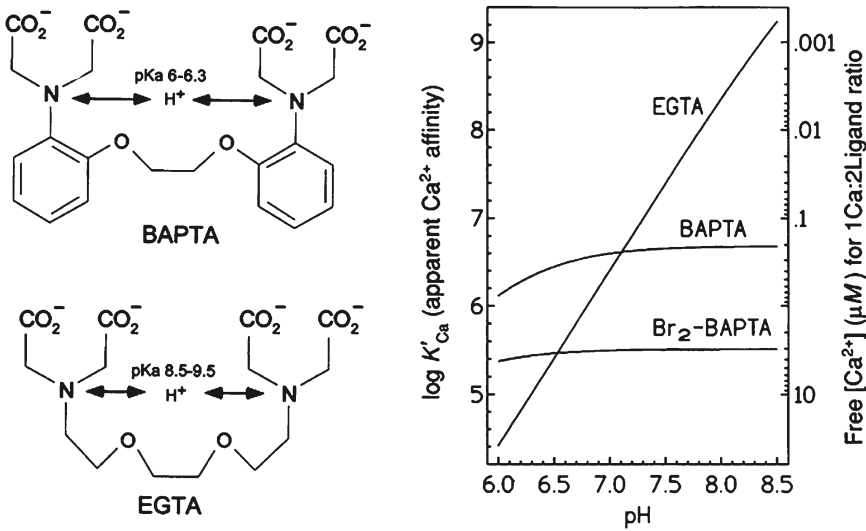


Fig. 3.1 Chemical structure and pH dependence of Ca²⁺ affinity of BAPTA and EGTA.

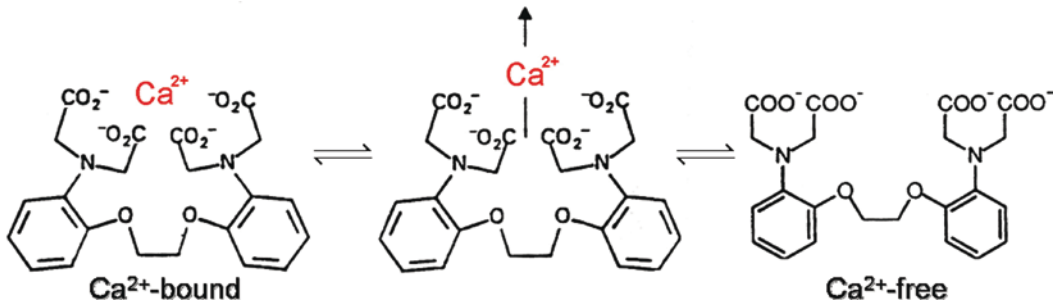
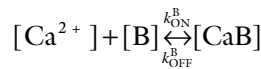


Fig. 3.2. Mechanism of Ca²⁺ chelation by BAPTA. The presence of four carboxylic acid (usually written as -COOH) functional groups makes possible the binding of Ca²⁺ ions.



and the corresponding kinetic equation is

$$\frac{d[\text{CaB}]}{dt} = k_{\text{ON}}^{\text{B}} [\text{Ca}^{2+}] [\text{B}] - k_{\text{OFF}}^{\text{B}} [\text{CaB}], \quad (3.1)$$

where square brackets are used to indicate concentration, k_{ON}^{B} is the rate constant for Ca²⁺ binding to B and $k_{\text{OFF}}^{\text{B}}$ is the rate constant for Ca²⁺ dissociation. At chemical equilibrium

$$\frac{d[\text{CaB}]}{dt} = 0$$

therefore

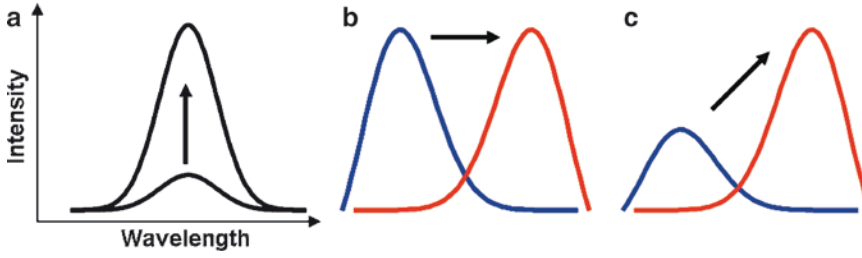


Fig. 3.3. Spectral properties that can be utilized to measure Ca²⁺ concentration.

$$\frac{[\text{Ca}^{2+}][\text{B}]}{[\text{CaB}]} = \frac{k_{\text{OFF}}^{\text{B}}}{k_{\text{ON}}^{\text{B}}} \equiv k_{\text{D}}^{\text{B}}. \quad (3.2)$$

In the above equation, which represents an instance of the law of mass action under equilibrium conditions, k_{D}^{B} is the equilibrium or dissociation constant (for BAPTA: $k_{\text{D}}^{\text{B}} = 0.192 \mu\text{M}$ (1); $k_{\text{ON}}^{\text{B}} = 500 \mu\text{M}^{-1} \text{s}^{-1}$ (2); $k_{\text{OFF}}^{\text{B}} = k_{\text{D}}^{\text{B}} \times k_{\text{ON}}^{\text{B}} = 96 \text{s}^{-1}$ (3)).

Ca²⁺-selective fluorescent probes share a modular design consisting of a metal-binding site (or sensor) B covalently coupled to a fluorophore A therefore:

$$[\text{A}] = [\text{B}]. \quad (3.3)$$

In order for such a fluorescent probe to provide useful information about its environment, it is necessary that its spectral properties be altered in a suitable manner by the parameter to be measured. For most biological applications, any one of the following three property changes is appropriate (Fig. 3.3):

- (a) A change in fluorescence yield
- (b) A shift in the excitation or emission spectrum
- (c) A combination of the two

2. Single Wavelength Indicators

Case (a) comprises the Fluo family of the so-called *single wavelength* fluorescent Ca²⁺ indicators (Fig. 3.4). The green-fluorescent emission (~525 nm) of Ca²⁺-bound fluo-3 is conventionally detected using optical filter sets designed for fluorescein (FITC). Fluo-4 is an analog of fluo-3 with the two chlorine substituents replaced by fluorine atoms.

Fluo-3 is essentially non-fluorescent unless bound to Ca²⁺ and exhibits an at least 100-fold Ca²⁺-dependent fluorescence enhancement (Fig. 3.5). The fluorescence quantum yields of Ca²⁺-bound fluo-3 and fluo-4 are essentially identical (~0.14 at saturating Ca²⁺).

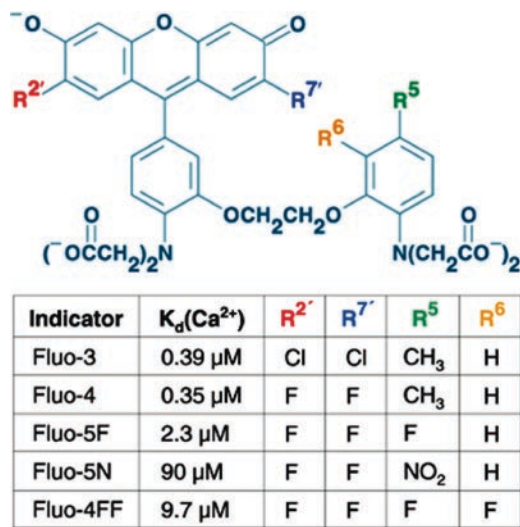


Fig. 3.4. Chemical structure and dissociation constants for the Fluo family of Ca^{2+} indicators.

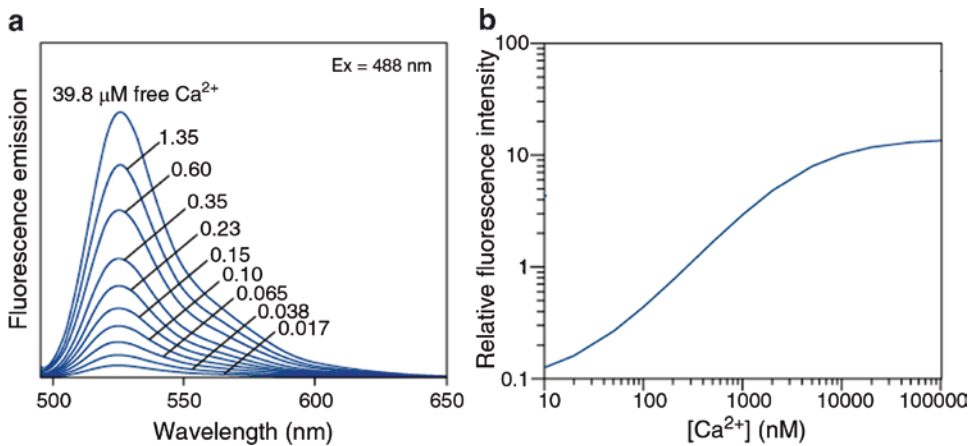
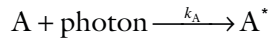


Fig. 3.5. (a) Fluo-3 spectra, excited by the 488-nm line of the Argon laser, are shown for different values of the free Ca^{2+} concentration ($[\text{Ca}^{2+}]$). (b) Relative fluorescence emission intensity, measured at the peak of each spectrum in (a), plotted against the corresponding $[\text{Ca}^{2+}]$.

The intact acetoxymethyl (AM) ester derivative of fluo-3 is also nonfluorescent. The absorption maximum of fluo-4 is blue-shifted about 12 nm when compared to fluo-3, resulting in an increased fluorescence excitation at 488 nm and consequently higher signal levels for confocal laser-scanning microscopy. When fluo-4 is substituted for fluo-3 (i.e., using identical loading protocols), fluorescence signals are at least doubled. The stronger fluorescence signals provided by fluo-4 are particularly advantageous in most cell types.

Also shown in Fig. 3.5b is the typical sigmoid dependence of the fluorescence emission on $[\text{Ca}^{2+}]$ (the free calcium concentration), which limits the useful detection range to approximately one log unit to the left and the right of the k_D^B . In particular, as is the case with other high affinity indicators, the upper limit for Fluo-3 and Fluo-4 is not exceeding 1–2 μM . Demonstrations that intracellular (i) free- Ca^{2+} concentrations ($[\text{Ca}^{2+}]_i$) can reach levels as high as 100 μM have sparked interest in fluorescent Ca^{2+} indicators (e.g. Fluo-5F, Fluo-5 N, Fluo-4FF), which can be used to measure calcium concentrations in the micromolar range (Fig. 3.4).

Suppose now that we have a system of fluorophores A at a total concentration c_T , which we excite with light of a given intensity and wavelength λ , (i.e. energy $h\nu$, where h is the Plank constant and ν is frequency). We can represent the excitation process as



where k_A is the excitation rate constant (with units of s^{-1}) and A^* represents fluorophores in the excited state. The system comes back down either non-radiatively (nr), with a rate k_{nr} , or radiatively (r), i.e. emitting a photon of longer wavelength (i.e. reduced energy $h\nu'$) with a rate constant k_r (Fig. 3.6).

The overall de-activation rate constant k_M is given by

$$k_M = k_r + k_{nr} = \frac{1}{\tau_{ex}}$$

(with units of s^{-1}) where τ_{ex} is the excited state lifetime (typically few ns). Under constant illumination conditions, a steady state is rapidly reached such that

$$k_A \alpha (c_T - [\text{A}^*]) = k_M [\text{A}^*], \quad (3.4)$$

where the dimensionless parameter α represents the fraction of absorbed photons. Therefore, the equilibrium (steady state) concentration of excited state fluorophores $[\text{A}^*]_{eq}$ is given by

$$[\text{A}^*]_{eq} = \frac{\alpha c_T}{\alpha + k_M / k_A},$$

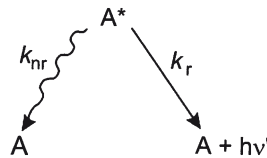
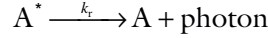


Fig. 3.6. Radiative and nonradiative decay from the excited state.

where, in general, $k_M \ll k_A$. The fluorescence emission intensity $F(t)$ is proportional to the number of photons emitted in the process of return from the excited state



therefore, its steady state value is

$$F = k_r [A^*]_{\text{eq}} = \frac{\alpha k_r c_T}{\alpha + k_M/k_A} \quad (3.5)$$

where the result is expressed in mols of photons emitted per unit time and per unit volume of dye solution.

For a given c_T , α is proportional to the product $\varepsilon(\lambda)l$ where $\varepsilon(\lambda)$ is the molar absorption coefficient (with units of $\text{L mol}^{-1} \text{m}^{-1}$) and l is the length of absorbing medium traversed by the illuminating beam. The fluorescence quantum yield (sometimes incorrectly termed quantum efficiency) is a gauge for measuring the efficiency of fluorescence emission relative to all of the possible pathways for relaxation and is generally expressed as

$$\eta_F = \frac{k_r}{k_M} \quad (3.6)$$

We thus conclude that F depends on factors such as illumination intensity, molar concentration of fluorescent probes, fluorescence quantum yield, molar absorption coefficient, and path length.

Let us then assume that the concentration of Ca^{2+} -selective fluorescent probes is kept low enough that the relationship between fluorescence emission intensity and concentration is indeed linear, as predicted by (3.5). In general, the concentration $[B]$ and $[CaB]$ of the Ca^{2+} -free (f) and Ca^{2+} -bound (b) forms differ with respect to quantum yield and absorption. Therefore, we write F as a linear combination

$$F = S_f[B] + S_b[CaB], \quad (3.7)$$

where the proportionality constants S_f, S_b lump all (system-dependent) factors such as illumination intensity, η_F , $\varepsilon(\lambda)$ and l . We are interested in measuring $[\text{Ca}^{2+}]$ in a closed system (e.g. the cell cytoplasm). Hence, we must also include the mass balance equation

$$c_T = [B] + [CaB]. \quad (3.8)$$

We then define

$$F_{\text{max}} = S_b c_T \quad (3.9)$$

as the fluorescence emission under Ca^{2+} saturation conditions and

$$F_{\text{min}} = S_f c_T \quad (3.10)$$

as the corresponding emission under Ca²⁺-free conditions (see Fig. 3.5).¹ Thus, the expression for F can be re-written as

$$F = F_{\min} + (S_b - S_f)[CaB] = F_{\max} - (S_b - S_f)[B].$$

Therefore, we can then also write

$$F - F_{\min} = (S_b - S_f)[CaB], \quad F_{\max} - F = (S_b - S_f)[B],$$

yielding

$$\frac{F - F_{\min}}{F_{\max} - F} = \frac{[CaB]}{[B]}.$$

At chemical equilibrium (3.2),

$$[Ca^{2+}] = k_D^B \frac{[CaB]}{[B]}.$$

Therefore, we conclude that

$$[Ca^{2+}] = k_D^B \frac{F - F_{\min}}{F_{\max} - F}. \quad (3.11)$$

Equation (3.11) expresses a quantitative relationship between the physiologically relevant equilibrium $[Ca^{2+}]$, the dissociation constant k_D^B and optically measurable quantities F_{\max} , F_{\min} and F for single wavelength Ca²⁺ selective probes such as Fluo-3 (Fig. 3.7). However, there are a number of caveats and problems with the practical use of (3.11).

First, we note that the denominator vanishes as $F \rightarrow F_{\max}$. Consequently, even small fluctuations in the estimate of F (due, e.g. to instrumental noise) may cause unacceptably large fluctuations in the estimate of $[Ca^{2+}]$ (unreliable zone in Fig. 3.7). Furthermore, (3.11) is difficult to apply to imaging experiments where F_{\max} , F_{\min} and F change rapidly over time due to photo-bleaching (see, e.g. Fig. 2 of (4)).

Provided that adverse effects are kept under control, (3.11) can be used to estimate the change in concentration

$$\Delta[Ca^{2+}] \equiv [Ca^{2+}] - [Ca^{2+}]_{\text{rest}}$$

caused, e.g., by a physiological stimulus, where

$$[Ca^{2+}] = k_D^B \frac{F - F_{\min}}{F_{\max} - F}$$

and F_0 are, respectively, the pre-stimulus free Ca²⁺ concentrations and fluorescence emission intensity. For stimuli that keep $[Ca^{2+}]$

¹ Note that, because of (3.3), the c_T in (3.4) is the same as in (3.8)–(3.10).

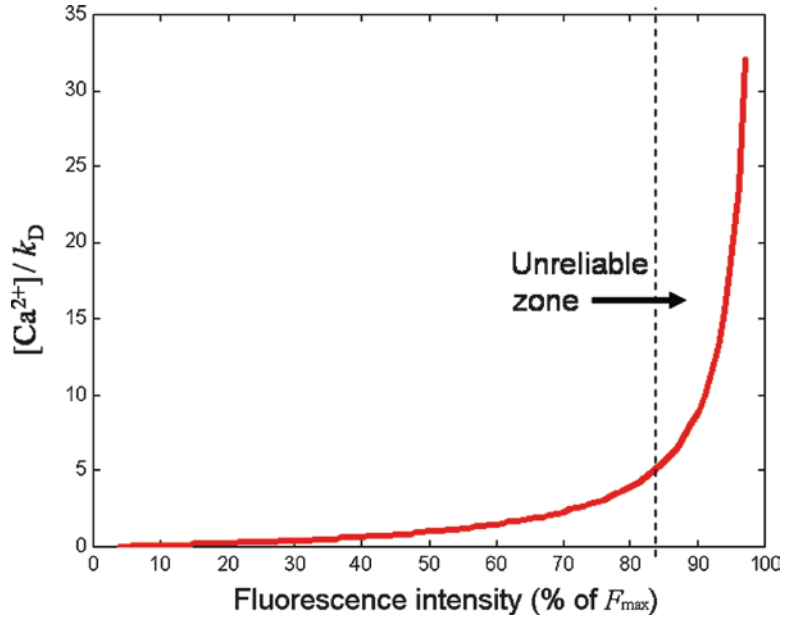


Fig. 3.7. Graphical representation of the single wavelength $[Ca^{2+}]$ -measurement formula.

within the approximately linear region of (3.11) (i.e., outside the unreliable zone) we can approximate $\Delta[Ca^{2+}]$ as

$$\Delta[Ca^{2+}] \cong \left. \frac{d[Ca^{2+}]}{dF} \right|_{F_0} (F - F_0),$$

that is

$$\Delta[Ca^{2+}] \cong k \frac{\Delta F}{F_0}, \quad (3.12)$$

where

$$k = k_D^B \frac{F_0 \cdot (F_{\max} - F_{\min})}{(F_{\max} - F_0)^2}.$$

Thus, if imaging experiments are performed in such a way that bleaching is moderate and as long as the total Ca^{2+} -sensor/fluorescent dye concentration c_T and the path length l do not change during the measurement, the *pixel-by-pixel ratio*

$$\frac{\Delta F}{F_0} = \frac{F - F_0}{F_0} \quad (3.13)$$

yields a unique function of $\Delta[Ca^{2+}]$, i.e. of the stimulus-induced change in the free Ca^{2+} concentration.

3. Ratiometric indicators

Calibration problems associated with the estimate of F_{\max} , F_{\min} and F are alleviated by the use of ratiometric (or dual wavelength) Ca²⁺ probes (Fig. 3.3b, c) such as fura-2 for the high affinity case or mag-Fura-2 (furaptra), Fura-2FF, and BTC for the low affinity case (5). Consider, for example, the excitation spectrum of fura-2 (Fig. 3.8).

The most remarkable feature is the existence of an *isosbestic point* at ~360 nm for which fluorescence is independent of [Ca²⁺]. Consequently, spectral amplitudes increase with increasing [Ca²⁺] to the left of the isosbestic point and decrease to the right. Consider then what happens to the fluorescence emission recorded, e.g., at the peak of the fura-2 emission spectrum (510 nm) in response to a hypothetical stimulus that causes a step-like increase in [Ca²⁺] (Fig. 3.9).

The traces in Fig. 3.9 represent idealized fura-2 readout vs. time of the [Ca²⁺] averaged within a region of interest (ROI) where the step-like increase is spatially uniform (for a more appropriate description of kinetics, see Sect. 4). As bleaching affects similarly the readout at all wavelengths, its effects can be neutralised by ratioing, e.g., λ_1/λ_0 or λ_1/λ_2 (Fig. 3.10).

Figure 3.10 also shows that taking the signal ratios for wavelengths on opposite sides of the isosbestic point (e.g. λ_1/λ_2) maximises the dynamic range, and therefore (optics transmittance permitting) should be preferred over ratioing with respect to the (isosbestic point) λ_0 signal.

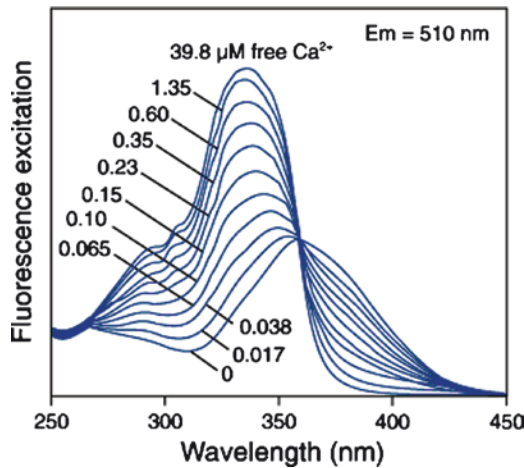


Fig. 3.8. Excitation spectra of fura-2 for the indicated values of the free Ca²⁺ concentration.

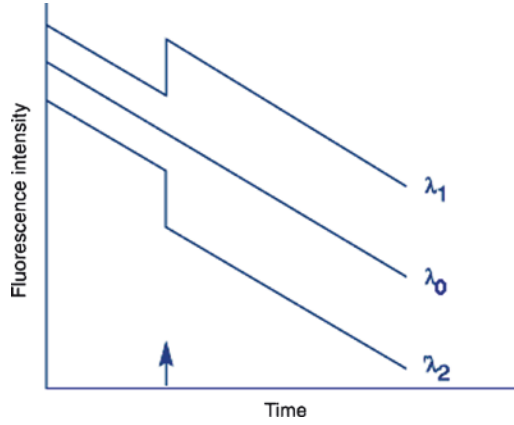


Fig. 3.9. Effect of a hypothetical step-like increase in $[Ca^{2+}]$ (whose occurrence is marked by the *vertical arrow*) in the presence of substantial bleaching of fura-2. λ_0 , excitation wavelength coincident with the isosbestic point; λ_1 , excitation wavelength to the left of the isosbestic point; λ_2 , excitation wavelength to the right of the isosbestic point.

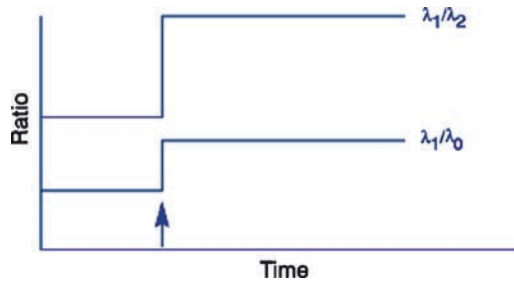


Fig. 3.10. Ratioing the signals acquired at different wavelengths cancels the effects of photobleaching.

We shall now derive a formula that allows quantifying the equilibrium $[Ca^{2+}]$ in terms of ratio signals.

Two excitation wavelengths λ_1, λ_2 and two dye species, free and bound, require four proportionality coefficients, hereby symbolized as S_{f1} for free dye measured at wavelength λ_1 , S_{f2} for free dye at λ_2 , and S_{b1}, S_{b2} for Ca^{2+} -bound dye at λ_1 and λ_2 , respectively (typical values for fura-2 are $\lambda_1 = 340$ nm and $\lambda_2 = 380$ nm; Fig. 3.11).

Then, we may write

$$F_1 = S_{f1} [B] + S_{b1} [CaB], \quad F_2 = S_{f2} [B] + S_{b2} [CaB]. \quad (3.14)$$

Using the law of mass action at equilibrium (3.2), we can express $[CaB]$ in (3.14) in terms of $[B]$ and $[Ca^{2+}]$ as

$$[CaB] = [Ca^{2+}] [B] / K_D^B.$$

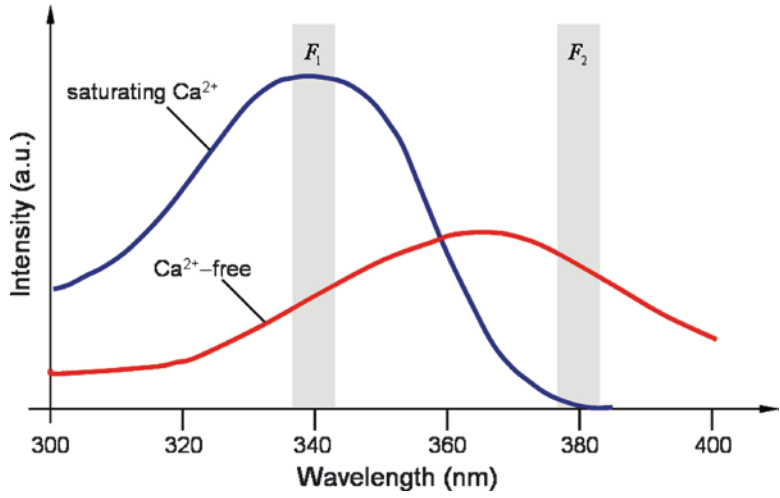


Fig. 3.11. Excitation spectra of fura-2 under Ca²⁺-free and saturation Ca²⁺ conditions.

Thus, factoring out the [B] term from (3.14), and taking the ratio signal as

$$R = \frac{F_1}{F_2},$$

yields

$$R = \frac{S_{f1} + S_{b1}[\text{Ca}^{2+}] / k_D^B}{S_{f2} + S_{b2}[\text{Ca}^{2+}] / k_D^B}.$$

The minimum value of the above expression achieved under Ca²⁺-free conditions is

$$R_{\min} = \frac{S_{f1}}{S_{f2}}, \quad (3.15)$$

Whereas, the maximum value achieved under saturating Ca²⁺ conditions is

$$R_{\max} = \frac{S_{b1}}{S_{b2}}. \quad (3.16)$$

We may thus re-express R in terms of R_{\min} and R_{\max} as

$$[\text{Ca}^{2+}] = k_D^B \left(\frac{R - R_{\min}}{R_{\max} - R} \right) \left(\frac{S_{f2}}{S_{b2}} \right), \quad (3.17)$$

which is known as the Grynkiewicz equation (6) (Fig. 3.12) and has a form closely analogous to (3.11). In particular, it displays a

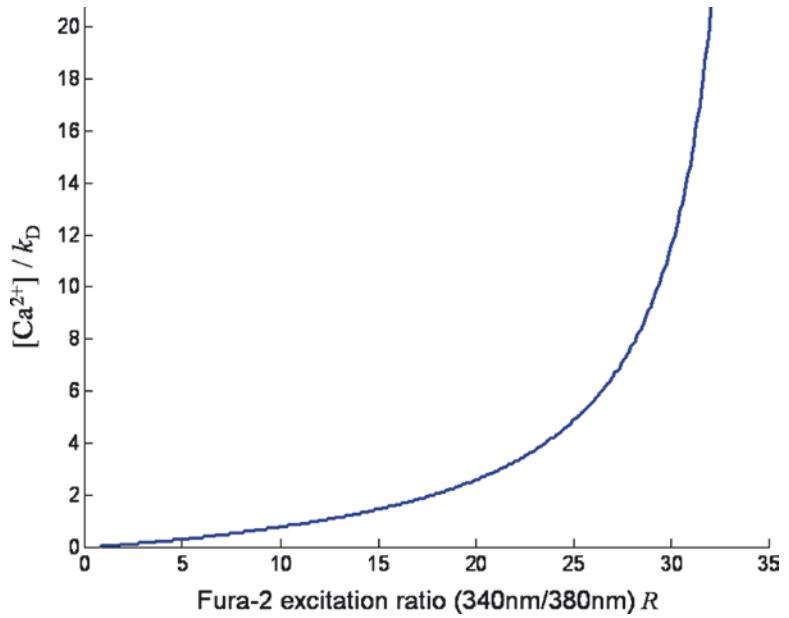


Fig. 3.12. Graphical representation of the Grynkiewicz equation for $\lambda_1 = 340$ nm and $\lambda_2 = 380$ nm, and reported values $R_{\min} = 0.768$, $R_{\max} = 35.1$, $S_{f2}/S_{b2} = 2.01$ and $k_D = 0.250 \mu\text{M}$ (6)..

hyperbolic singularity for $R = R_{\max}$ which makes the estimate of $[\text{Ca}^{2+}]$ problematic when $[\text{Ca}^{2+}]$ exceeds the k_D^B by more than ~ 5 -fold (the actual viability range depends on the available signal to noise ratio). However, using ratios and (3.17), dye content and instrumental sensitivity are free to change between one ratio and another since they cancel out in each ratio. Of course, stability is still required within each individual ratio measurement. Also R , R_{\min} , R_{\max} and S_{f2}/S_{b2} should all be measured on the same instrumentation so that any wavelength biases influences all of them equally.

Thus, though not as large as that of fluo-3 (~ 100), the dynamic range of fura-2 is a remarkable $R_{\max}/R_{\min} \sim 45$. Detailed calibration procedures are described in (7).

Note that (3.17) applies equally well to emission ratios of dyes such as indo-1 (Fig. 3.13a). With minor modifications, the versatile (3.17) accommodates also other dual emission approaches to $[\text{Ca}^{2+}]$ measurement, e.g. dye mixtures such as fluo-3 and fura red (8) (Fig. 3.13b) or fluorescent resonance energy transfer (FRET)-based genetically encoded calcium indicators (GECIs), such as: cameleons (9–11); troponin-C based biosensors (12); or D3cpv (13,14).

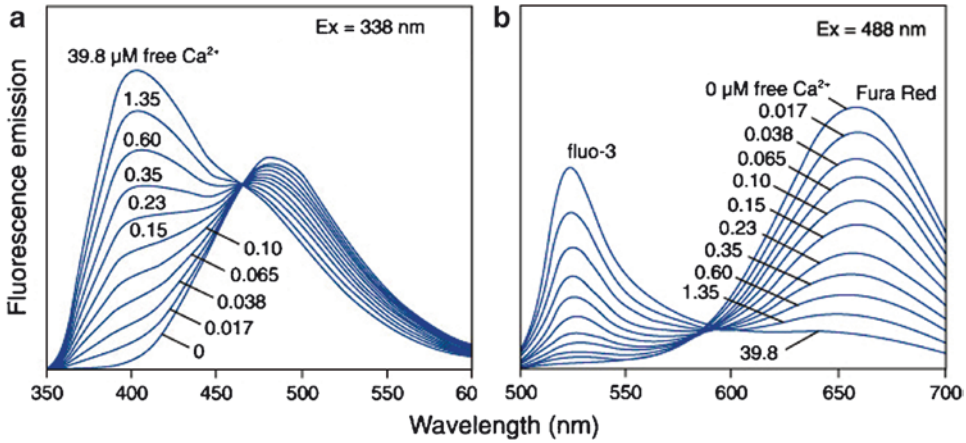
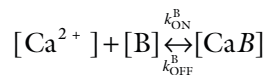


Fig. 3.13. Emission spectra of (a) indo-1 and (b) a mixture of fluo-3 and fura red, for the indicated values of the free Ca²⁺ concentration.

4. Displacement from Equilibrium

The endogenous buffers normally present inside the cell bind most of the Ca²⁺ that enters the cytoplasm through Ca²⁺ permeable channels. However, because these buffers are relatively immobile and may present with a lower affinity for Ca²⁺, addition of a mobile high-affinity buffer such as fura-2 allows the exogenous buffer to out-compete these endogenous buffers and alter the nature of the *transient* intracellular free calcium ([Ca²⁺]_i) signals (15). Dramatic examples of how buffering effects alter the time course of fluorescence emission of fura-2 are presented in Fig. 2A and Fig. 3A of (16). Indeed, the key factor in (3.11), (3.12), and (3.17), which are all equilibrium equations based on (3.2) is the dissociation constant k_D^B , i.e. the ratio k_{OFF}^B/k_{ON}^B . By contrast under dynamic, i.e. non-equilibrium conditions, the shape of the fluorescence signals evoked by [Ca²⁺] transients depends on each one of the factors k_{OFF}^B , k_{ON}^B and c_T . Thus, for a binding reaction between Ca²⁺ and the indicator the rate of approach to equilibrium can vary even for indicators with the same k_D^B . Therefore, a better description of kinetics is the relaxation time τ , which describes how fast a reaction comes to a new equilibrium when one or more of the reactants is suddenly shifted away from its equilibrium concentration. To define τ precisely, consider again the binding reaction



with the initial equilibrium concentrations $[Ca^{2+}]_0$, $[B]_0$, $[CaB]_0$. If the system is perturbed, the transiently shifted concentrations

$[\text{Ca}^{2+}]$, $[\text{B}]$, $[\text{CaB}]$ will come rapidly to a new equilibrium $[\text{Ca}^{2+}]_1$, $[\text{B}]_1$, $[\text{CaB}]_1$. We therefore define a quantity Δx , which represents the difference between the shifted concentrations and the new equilibrium concentrations that is

$$\Delta x = [\text{Ca}^{2+}] - [\text{Ca}^{2+}]_1 = [\text{B}] - [\text{B}]_1 = [\text{CaB}]_1 - [\text{CaB}].$$

Next, consider the reaction equation for one of the reactants, e.g., $[\text{Ca}^{2+}]$:

$$\frac{d[\text{Ca}^{2+}]}{dt} = k_{\text{OFF}}^{\text{B}}[\text{CaB}] - k_{\text{ON}}^{\text{B}}[\text{Ca}^{2+}][\text{B}],$$

which can be re-written in term of Δx as

$$\frac{d\Delta x}{dt} = k_{\text{OFF}}^{\text{B}}([\text{CaB}]_1 - \Delta x) - k_{\text{ON}}^{\text{B}}([\text{Ca}^{2+}]_1 + \Delta x)([\text{B}]_1 + \Delta x)$$

or

$$\begin{aligned} \frac{d\Delta x}{dt} = & - \left\{ k_{\text{OFF}}^{\text{B}} + k_{\text{ON}}^{\text{B}}([\text{Ca}^{2+}]_1 + [\text{B}]_1) \right\} \Delta x + k_{\text{OFF}}^{\text{B}}[\text{CaB}]_1 \\ & - k_{\text{ON}}^{\text{B}}[\text{Ca}^{2+}]_1[\text{B}]_1 - k_{\text{ON}}^{\text{B}}\Delta x^2 \end{aligned}$$

But, $[\text{Ca}^{2+}]_1$, $[\text{B}]_1$, $[\text{CaB}]_1$ are equilibrium values, therefore,

$$k_{\text{OFF}}^{\text{B}}[\text{CaB}]_1 - k_{\text{ON}}^{\text{B}}[\text{Ca}^{2+}]_1[\text{B}]_1 = 0.$$

Furthermore, for sufficiently small changes

$$\Delta x \ll [\text{Ca}^{2+}]_1 + [\text{B}]_1$$

the quadratic term can be neglected and the rate of change of Δx can be approximated by the equation

$$\frac{d\Delta x}{dt} \cong -k_s \Delta x, \quad (3.18)$$

where the rate constant of the reaction, k_s (with units of s^{-1}), is

$$k_s \equiv \frac{1}{\tau} = k_{\text{ON}}^{\text{B}}([\text{Ca}^{2+}]_1 + [\text{B}]_1) + k_{\text{OFF}}^{\text{B}}. \quad (3.19)$$

For example:

fura-2 on-rate $6.0 \times 10^8 \text{ M}^{-1} \text{ s}^{-1}$ off-rate 98 s^{-1}

fura-2 on-rate $7.5 \times 10^8 \text{ M}^{-1} \text{ s}^{-1}$, off-rate $26,760 \text{ s}^{-1}$

The prediction that furaptra should be much faster than fura-2 is verified experimentally (Fig. 3.14), lending support to the argument used in the derivation of (3.18) and (3.19). Consider then what happens in a typical experiment that rapidly and markedly displaces $[\text{Ca}^{2+}]$ from its equilibrium value as shown,

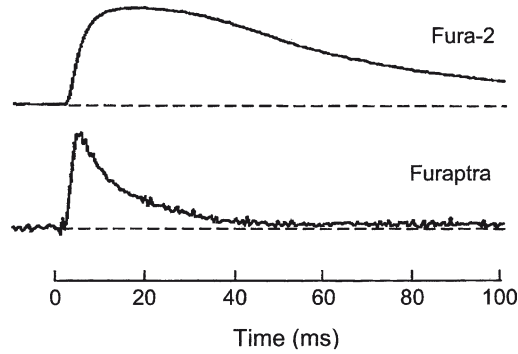


Fig. 3.14. Response to a brief Ca²⁺ influx event, scaled to the same peak amplitude, monitored in muscle cells with high affinity Ca²⁺-indicator fura-2 and low affinity indicator fura-2/ura (modified from Fig. 1.9 of (44)).

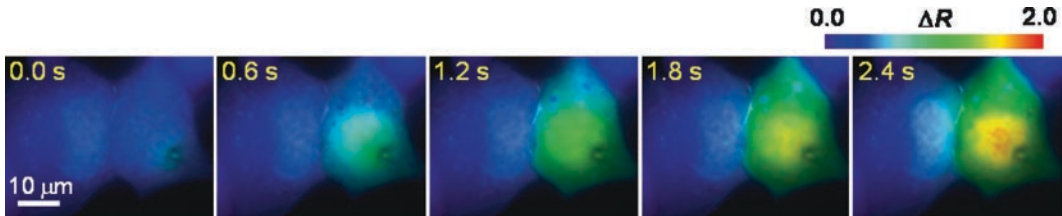


Fig. 3.15. At time $t=0.0$ s a glass micropipette starts to deliver IP₃ into the cytoplasm of the right cell under whole-cell patch clamp conditions. While IP₃ diffuses along its concentration gradient, Ca²⁺ is mobilised from intracellular stores of both cells, with different time courses. Pseudo colours encode the pixel-by-pixel fura-2 ratio change $\Delta R = R - R_0$, where R_0 indicates the pre-stimulus ratio, according to the colour-scale bar shown above. For further details, see (45).

for example, by the sequence of images in Fig. 3.15 collected from a pair of gap-junction coupled HeLa cells loaded with fura-2.

The key question to be asked (and answered!) whenever images of this sort are displayed is: how do the pseudo colours relate to the actual local [Ca²⁺]? Obviously, the matter is not limited to wide-field ratiometric images (Fig. 3.15), but encompasses also the encoding of fluorescence emission from single wavelength dyes, e.g., in confocal line scan experiments (Fig. 3.16).

Despite the countless abuses present in the literature, the very presence of spatial and temporal [Ca²⁺] gradients which endow the rainbow-coloured pictures shown above with their (potentially) artistically attractive character implies that equilibrium formulae, e.g., (3.11), (3.12), and (3.17), simply *cannot* be used to quantify [Ca²⁺] under such non-equilibrium conditions. So, what needs to be done if one is to step out of the *pretty pictures* trap using optically measurable quantities to actually estimate [Ca²⁺] across time and space?

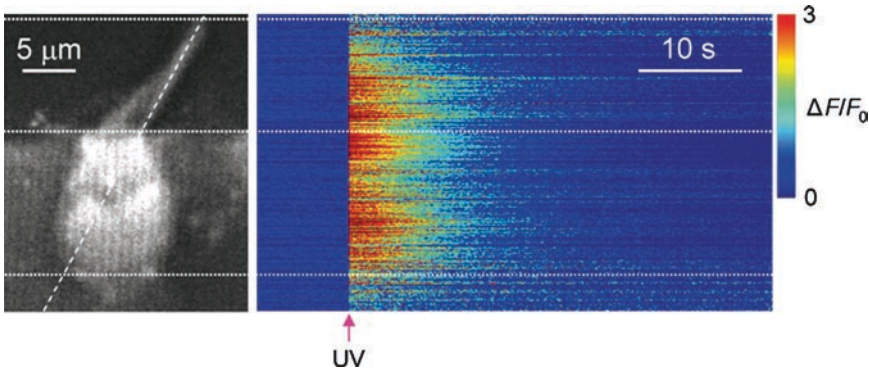


Fig. 3.16. *Left*: confocal image of baseline Fluo-4 fluorescence of a hair cell in an organotypic culture of mouse utricular macula. The diagonal dashed line represents the scan line during subsequent data acquisition. The hair bundle comprises the top and middle horizontal dotted lines (the latter crosses the cell cuticular plate). The cell soma comprises middle and lower lines. *Right*: in this line-scan image, ordinates are pixel positions along the scan line, abscissa is time and fluorescence transients, $\Delta F/F_0$, evoked by a 4-ns UV pulse (arrow), are color-coded according to the color scale-bar at right. Signals from pixels below the lowermost horizontal dotted line arise from adjacent cells. For further details, see (46).

5. Ca^{2+} Dynamics

Temporary and localized fluxes of Ca^{2+} ions entering the cytosol are responsible for carrying information to cellular targets in their micro-environment (Ca^{2+} *microdomains*), creating a dynamic situation where Ca^{2+} concentration is rapidly lowered by a number of intracellular mechanisms (basic mechanisms are represented in Fig. 3.17).

Besides passive diffusion of Ca^{2+} away from its site of action and buffering by variety of Ca^{2+} binding proteins, control mechanisms include the action of Ca^{2+} -ATPases (PMCA and SERCA pumps) as well as Na^+ - Ca^{2+} exchangers (NCX) (17). Ca^{2+} signals are also amplified by Ca-induced Ca-release (CICR) mediated by ryanodine receptors (RyRs) and $\text{Ins}(1,4,5)\text{P}_3$ receptors (IP_3Rs) in the membrane of the endoplasmic/sarcoplasmic reticulum (ER/SR) (18,19). Other mechanisms, such as voltage- and or ligand-gated Ca^{2+} -permeable channels in the plasma membrane may be at play, serving specialised cell functions.

A mathematical description of Ca^{2+} -related mechanisms provides the only way to estimate the $[\text{Ca}^{2+}]_i$ when the system is far from the equilibrium. In this case, the law of mass action (3.1) for Ca^{2+} and one (representative) endogenous buffer C becomes:

$$\frac{\partial [\text{Ca}^{2+}]_i}{\partial t} = k_{\text{OFF}}^{\text{C}} [\text{CaC}] - k_{\text{ON}}^{\text{C}} [\text{Ca}^{2+}]_i [\text{C}] + J, \quad (3.20)$$

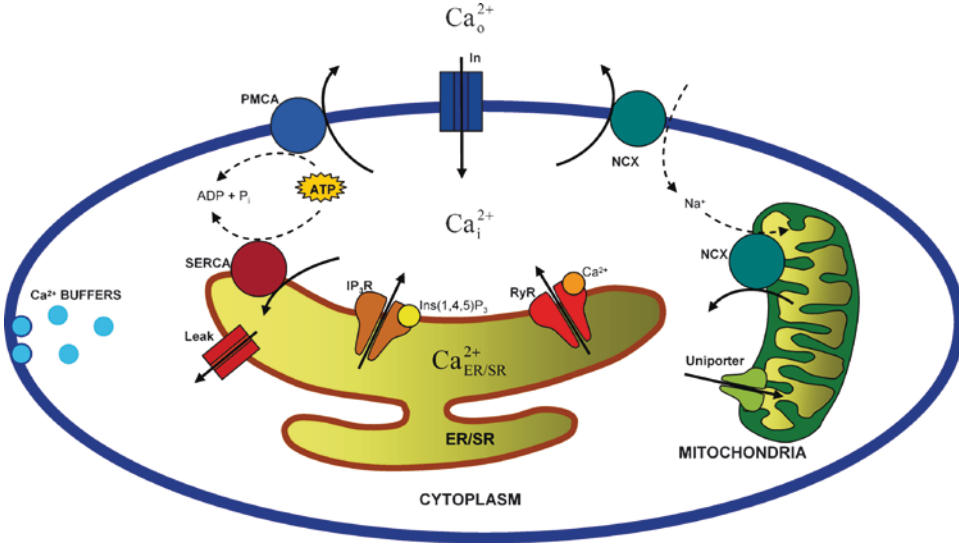


Fig. 3.17. Basic elements involved in Ca²⁺ signalling in eukaryotic cells.

where t is time, $[C]$ and $[CaC]$ are the concentrations of free buffer and Ca²⁺ bound to buffer, respectively. J (in M/ s⁻¹), the sum of the different Ca²⁺ fluxes entering/exiting the cytoplasm is a function of Ca²⁺ concentrations in various compartments and possibly other variables, e.g., IP₃ concentration. As for the latter, the opening of the IP₃Rs is modulated by IP₃, the binding of which increases the sensitivity of the channel to the surrounding [Ca²⁺]_i. At high levels, cytoplasmic Ca²⁺ exerts a negative feedback action, decreasing the sensitivity to both IP₃ and Ca²⁺: as [Ca²⁺]_i rises, the channel begins to close again. The contribution to J due to flux of Ca²⁺ out of the calcium store (ER/SR) into the cytosol can be described by the equation

$$J_{ER} = [k_{LEAK} + k_{IP_3R}]([Ca^{2+}]_{ER/SR} - [Ca^{2+}]_i), \quad (3.21)$$

where k_{LEAK} (units of s⁻¹) describes Ca²⁺-leakage through the ER/SR channels and k_{IP_3R} is a function of both [Ca²⁺]_i and [IP₃] describing the IP₃ receptor kinetics. As mentioned above, other equations may have to be included in the description of J to account for the action of voltage- and/or ligand-gated Ca²⁺ permeable channels in the plasma membrane.

The increase of [Ca²⁺]_i due to Ca²⁺ influx is rapidly lowered by activation of SERCA and PMCA pumps, which accumulate Ca²⁺ in the ER/SR and outside the cell respectively. Pump action produces a negative Ca²⁺ flux (efflux) that can be included in J in the form

$$J_{\text{PUMP}} = -V_{\text{max}} \frac{[\text{Ca}^{2+}]_i^m}{[\text{Ca}^{2+}]_i^m + K_M^m}, \quad (3.22)$$

where $V_{\text{max}} = n \cdot v$ is the pump maximum velocity (n is molar concentration of pump molecules and v the maximal turnover rate in s^{-1}), K_M is the *Michaelis* constant and the exponent m equals two for the SERCA pumps and one for the PMCAs (2, 20–22). Since the PMCA is capable of effectively binding Ca^{2+} even when its concentrations is quite low, it is better suited to the task of restoring the resting $[\text{Ca}^{2+}]_i$. This task is vital when considerable amount of Ca^{2+} enters periodically the cell, e.g., in hair cells (Fig. 3.18) depolarized by mechanical stimuli (due to sound or acceleration).

In general, Ca^{2+} entry is localized and close to cellular targets and thus generates Ca^{2+} concentration gradients within the cell. The spatial and temporal description of diffusion processes is provided by Fick's second law (23):

$$\frac{\partial [\text{Ca}^{2+}]_i}{\partial t} = D_{\text{Ca}} \cdot \Delta [\text{Ca}^{2+}]_i, \quad (3.23)$$

where

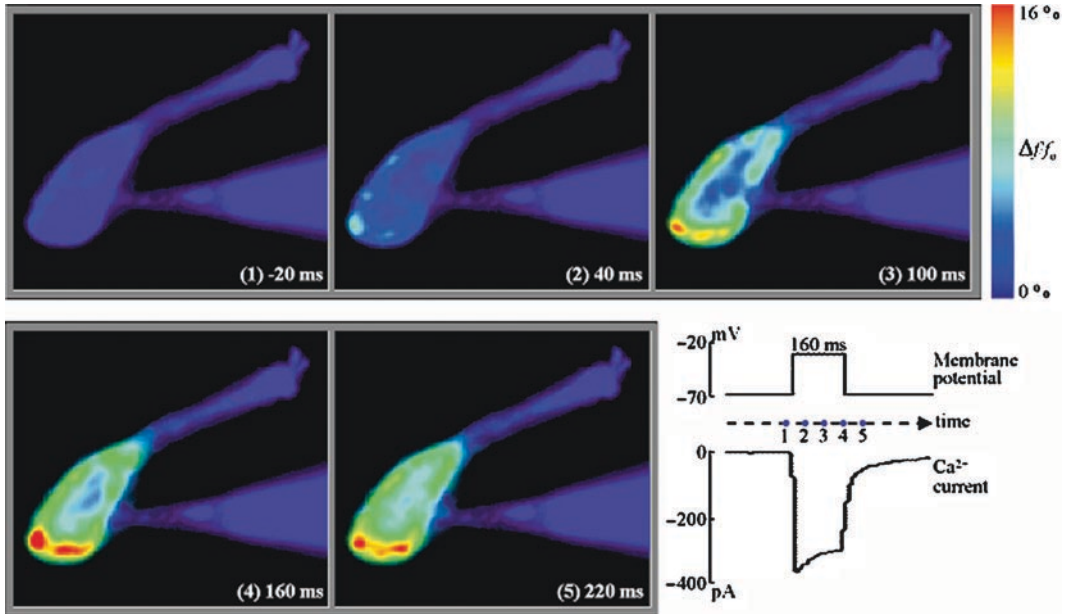


Fig. 3.18. Isolated hair cell from the frog crista ampullaris contacted by a patch pipette entering from the right and containing the membrane-impermeant Ca^{2+} -sensor Oregon Green 488 BAPTA-1. The hair cell was depolarized for 160 ms, from time zero, eliciting $[\text{Ca}^{2+}]_i$ transients near the active presynaptic zones (*hotspots*). Inward Ca^{2+} current through voltage-dependent Ca^{2+} channels ($\text{Ca}_v1.3$ type) was measured using a CsCl-based intracellular solution that selectively blocked K^+ currents (adapted from (47)).

$$\Delta = \frac{\partial^2}{\partial x^2} + \frac{\partial^2}{\partial y^2} + \frac{\partial^2}{\partial z^2}$$

is the Laplace operator and the dependence of $[\text{Ca}^{2+}]_i$ on spatial coordinates $\mathbf{r}=(x,y,z)$ and time t is understood. $D_{\text{Ca}} \cong 440 \mu\text{m}^2\text{s}^{-1}$ is the diffusion constant of Ca^{2+} in an aqueous medium with the viscosity of the cytosol (3).

Including the contribution due to Ca^{2+} diffusion (3.23) in (3.20) and considering the presence of an exogenous buffer B and an endogenous buffer C, yields the system of reaction–diffusion equations:

$$\begin{cases} \frac{\partial[\text{Ca}^{2+}]_i}{\partial t} = k_{\text{OFF}}^{\text{C}}[\text{CaC}] - k_{\text{ON}}^{\text{C}}[\text{Ca}^{2+}]_i[\text{C}] + D_{\text{Ca}} \cdot \Delta[\text{Ca}^{2+}]_i + J \\ \frac{\partial[\text{B}]}{\partial t} = k_{\text{OFF}}^{\text{B}}[\text{CaB}] - k_{\text{ON}}^{\text{B}}[\text{Ca}^{2+}]_i[\text{B}] + D_{\text{B}} \cdot \Delta[\text{B}] \\ \frac{\partial[\text{CaB}]}{\partial t} = -k_{\text{OFF}}^{\text{B}}[\text{CaB}] + k_{\text{ON}}^{\text{B}}[\text{Ca}^{2+}]_i[\text{B}] + D_{\text{CaB}} \cdot \Delta[\text{CaB}] \\ \frac{\partial[\text{C}]}{\partial t} = k_{\text{OFF}}^{\text{C}}[\text{CaC}] - k_{\text{ON}}^{\text{C}}[\text{Ca}^{2+}]_i[\text{C}] + D_{\text{C}} \cdot \Delta[\text{C}] \\ \frac{\partial[\text{CaC}]}{\partial t} = -k_{\text{OFF}}^{\text{C}}[\text{CaC}] + k_{\text{ON}}^{\text{C}}[\text{Ca}^{2+}]_i[\text{C}] + D_{\text{CaC}} \cdot \Delta[\text{CaC}] \end{cases} \quad (3.24)$$

where the diffusion coefficients of free buffers and Ca^{2+} -bound to buffers are almost equal. In particular, $D_{\text{C}}, D_{\text{CaC}}$ are between 70 and $90 \mu\text{m}^2\text{s}^{-1}$ for the three important Ca^{2+} buffers calbindin- $\text{D}_{28\text{K}}$, calretinin and parvalbumin (3) while $D_{\text{B}}, D_{\text{CaB}}$ are generally larger, e.g., $D_{\text{B}} = 220 \mu\text{m}^2\text{s}^{-1}$ for Oregon Green 488 BAPTA-1.

Thus, to estimate $[\text{Ca}^{2+}]_i$ as a function of $\mathbf{r}=(x,y,z)$ and t , one needs to solve the above system of equations (3.24). Classical methods to numerically solve (systems of) partial differential equations (PDEs), subdivide the solution space (e.g. the cytoplasm of the cell) in several compartments (*voxels* or *shells*) (24–27). Discretization of the Laplace operator then leads to a system of ordinary differential equations (ODEs) for each voxel/shell of the 3D diffusion volume (Fig. 3.19), which take into account the contribution to J due to the adjacent compartments.

Numerical solution of very large set of simultaneous ODEs is typical in Systems Biology and represents an important constraint in the choice of the model parameters. In fact, CPU time consumption increases as the third power of the spatial resolution, e.g., a reaction–diffusion space of $1 \mu\text{m}^3$ could be subdivided in 8,000 cubic voxels of side $L = 50 \text{ nm}$ or in 10^6 voxels of side $L = 10 \text{ nm}$.

An alternative approach to simulate molecular diffusion is the Monte Carlo method. This type of simulations, which are essentially based upon the repetitive generation of random numbers, have been used to study reaction and diffusion processes in biological systems (28–34) including Ca^{2+} dynamics (35–40).

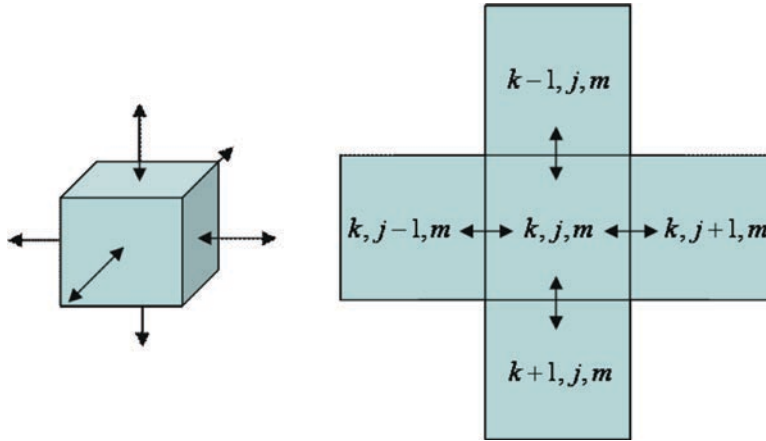


Fig. 3.19. Example of space discretization in cubic voxels. To solve (3.24) in the (k, j, m) indexed voxel we have to solve a system with further six equations corresponding to the orthogonal fluxes from the adjacent voxels.

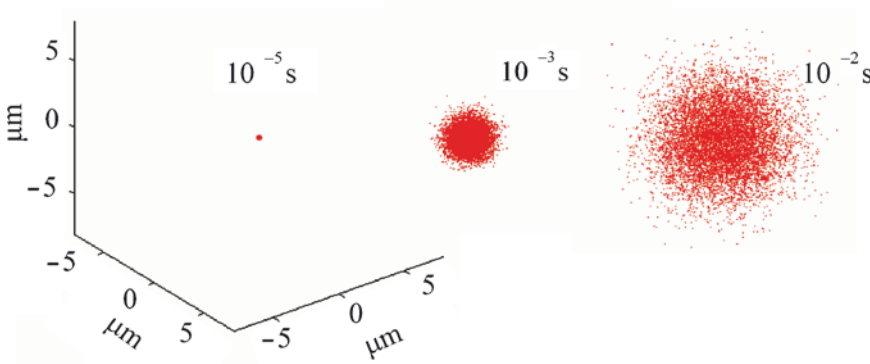


Fig. 3.20. Random walk simulation for 10^4 particles diffusing in an unlimited isotropic medium shown at three different times after the onset of diffusion from a point source.

The Monte Carlo algorithm can be exploited to approximate the Brownian motion of the real molecules (*random walk*) with that of a suitable number of *particles* (Fig. 3.20). One advantage of the method is also the possibility of simulating with great accuracy 3D diffusion in the presence of realistic boundaries (3).

The study of Ca^{2+} dynamics in living cells typically combines Ca^{2+} -sensitive fluorescent dyes, patch clamp and optical microscopy to produce images of the patterns of fluorescence of a Ca^{2+} indicator following various stimulation protocols. In the most favourable case, the only observable variable is a linear combination of the fluorescence emission of free dye and dye bound to Ca^{2+} . Thus, the most interesting unobservable variables such as $[\text{Ca}^{2+}]_i$ or $[\text{C}]$ (Fig. 3.21) must be deduced only after optimization by trial and error of the model free parameters with a fitting procedure of the model output to the experimental data.

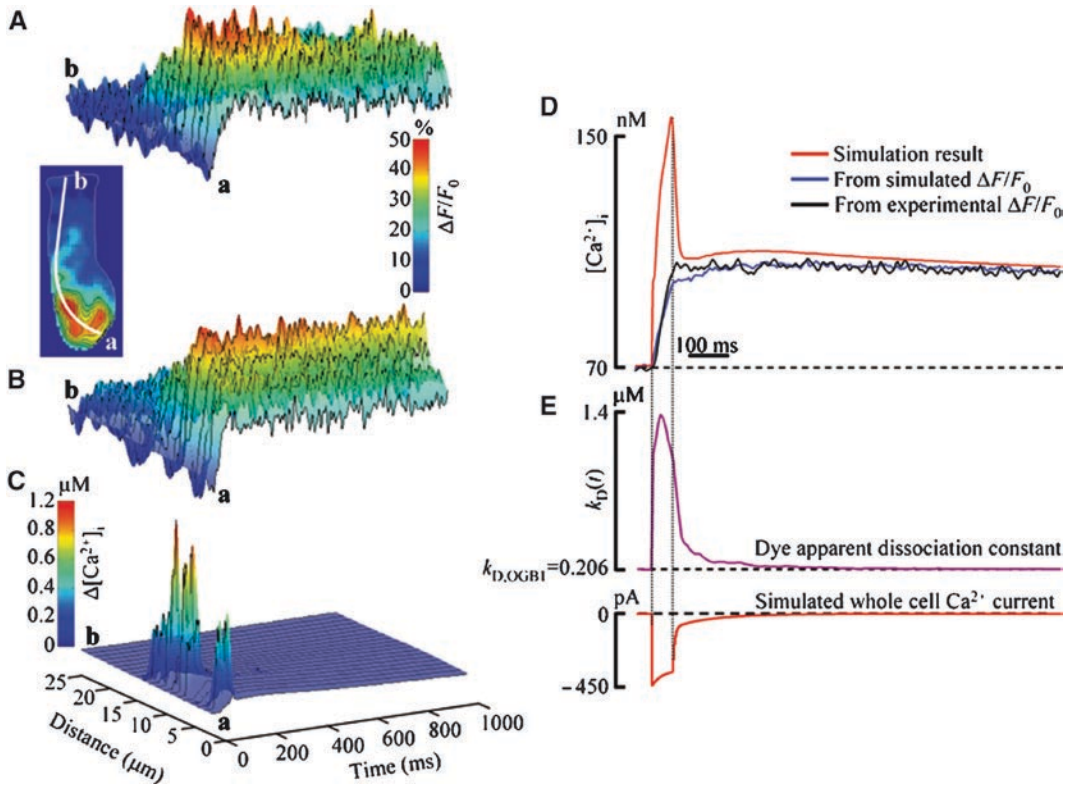


Fig. 3.21. Fluorescence signals appear as low pass filtered versions of the $[Ca^{2+}]_i$ in the presence of sustained Ca^{2+} influx. The model simulates the buffered diffusion of Ca^{2+} from presynaptic hotspots following 50-ms depolarization of the hair cell plasma membrane, reconstructed in three dimensions (3). (A) Pseudoline-scan representation of the experimental $\Delta F/F_0$ signal obtained with 50- μM Oregon Green 488 BAPTA-1; abscissas represent time and ordinates are distance along the *white line* (a–b) passing through a number of hotspots (*inset*). (B) Similar $\Delta F/F_0$ signals were obtained for the modelled cell containing 1.7 mM of a fast endogenous Ca^{2+} buffer. (C) $\Delta[Ca^{2+}]_i$ changes corresponding to the simulation in (B). (D) Time course of the simulated $[Ca^{2+}]_i$, integrated over the entire cell volume (*red trace*) and $[Ca^{2+}]_i$ values derived either from the simulated (*blue trace*) or from the experimental (*black trace*) $\Delta F/F_0$ whole cell signals, based on the law of mass action at equilibrium (3.11). (E) Average dissociation “constant” of the Oregon Green 488 BAPTA-1 dye (*top*) computed from (3.2) from the local simulated reactant concentrations accounts for the nonequilibrium of the system, perturbed by the whole cell Ca^{2+} current (*bottom*) due to cell depolarization. For further details of the model, see (3).

The original solution provided by the Monte Carlo model in (3) is the generation of a dye virtual fluorescence to be compared with that recorded during the experiments. At a given emission wavelength, the measured fluorescence signal F can be expressed by (3.7) as:

$$F = \bar{S}_f \cdot n_f + \bar{S}_b \cdot n_b, \quad (3.25)$$

where n_f is the number of free dye molecules and n_b is the number of dye molecules buffered to Ca^{2+} , \bar{S}_f and \bar{S}_b are proportional to S_f and S_b in (3.7), respectively.

By defining

$$\alpha = \bar{S}_b / \bar{S}_f = F_{\max} / F_{\min}, \quad (3.26)$$

we can write (3.25) as:

$$F = \bar{S}_f \cdot (\alpha n_b + n_f) \quad (3.27)$$

and

$$F_0 = \bar{S}_f \cdot (\alpha n_{b,0} + n_{f,0}) \quad (3.28)$$

where $n_{b,0}$ and $n_{f,0}$ are the numbers of dye molecules, respectively, bound to and free from Ca^{2+} before the Ca^{2+} stimulus.

Defining χ as the proportionality constant between the number n of real dye molecules and the corresponding number N of simulated particles, we can rewrite (3.27) and (3.28) as:

$$F = \chi \bar{S}_f \cdot (\alpha N_b + N_f)$$

and

$$F_0 = \chi \bar{S}_f \cdot (\alpha N_{b,0} + N_{f,0})$$

where $N_{b,0}$ and $N_{f,0}$ are the numbers of dye particles, respectively, bound to and free from Ca^{2+} before the (simulated) Ca^{2+} stimulus. The last two equations permit us to compute the useful quantity:

$$\frac{\Delta F}{F_0} = \frac{F - F_0}{F_0} = \frac{\alpha N_b + N_f - \alpha N_{b,0} - N_{f,0}}{\alpha N_{b,0} + N_{f,0}} \quad (3.29)$$

and thus to convert particle counts to simulated fluorescence signals. Note that the parameter α we used to generate the virtual $\Delta F/F_0$ signals is characteristic of the dye and is relatively insensitive to the experimental conditions, whereas the absolute values of F_{\max} and F_{\min} may vary from experiment to experiment. For example, Oregon Green 488 BAPTA-1 has $\alpha \cong 5$ (41) while for Fluo-4 $\alpha \cong 100$ (42).

It is also possible to include the effect of the poor axial resolution of wide field microscopy on $\Delta F/F_0$ by considering the relationship between the fluorescence intensity $F(z)$ due to a point source and the source distance, z , from the focal plane ($z=0$). In particular, the ratio $F(z)/F(0)$ can be estimated as shown in (43).

Acknowledgments

This work has been supported by grants to FM from Fondazione Cariparo (Progetti di Eccellenza 2006), MIUR PRIN Grant n. 2007BZ4RX3_003 and the European commission FP6 Integrated

Project EuroHear (LSHGCT20054512063) under the Sixth Research Frame Program of The European Union. We thank the Editor of this book, Alexej Verkhratsky, for discussions and constructive criticism.

References

1. Tsien RY (1980) New calcium indicators and buffers with high selectivity against magnesium and protons: design, synthesis, and properties of prototype structures. *Biochemistry* 19(11):2396–2404
2. Wu YC, Tucker T, Fettiplace R (1996) A theoretical study of calcium microdomains in turtle hair cells. *Biophys J* 71(5):2256–2275
3. Bortolozzi M, Lelli A, Mammano F (2008) Calcium microdomains at presynaptic active zones of vertebrate hair cells unmasked by stochastic deconvolution. *Cell Calcium* 44(2):158–168
4. Thomas D et al (2000) A comparison of fluorescent Ca²⁺ indicator properties and their use in measuring elementary and global Ca²⁺ signals. *Cell Calcium* 28(4):213–223
5. Hyrc KL, Bownik JM, Goldberg MP (2000) Ionic selectivity of low-affinity ratiometric calcium indicators: mag-Fura-2, Fura-2FF and BTC. *Cell Calcium* 27(2):75–86
6. Grynkiewicz G, Poenie M, Tsien RY (1985) A new generation of Ca²⁺ indicators with greatly improved fluorescence properties. *J Biol Chem* 260(6):3440–3450
7. Kao JPY (1994) Practical aspects of measuring [Ca²⁺] with fluorescent indicators. In: Nuccitelli R (ed) *A practical guide to the study of calcium in living cells*. Academic, San Diego, p 155–181
8. Lipp P, Niggli E (1993) Ratiometric confocal Ca(2+)-measurements with visible wavelength indicators in isolated cardiac myocytes. *Cell Calcium* 14(5):359–372
9. Miyawaki A et al (1997) Fluorescent indicators for Ca²⁺ based on green fluorescent proteins and calmodulin. *Nature* 388(6645):882–887
10. Truong K et al (2001) FRET-based in vivo Ca²⁺ imaging by a new calmodulin-GFP fusion molecule. *Nat Struct Biol* 8(12):1069–1073
11. Palmer AE, Tsien RY (2006) Measuring calcium signaling using genetically targetable fluorescent indicators. *Nat Protoc* 1(3):1057–1065
12. Heim N et al (2007) Improved calcium imaging in transgenic mice expressing a troponin C-based biosensor. *Nat Methods* 4(2):127–129
13. Wallace DJ et al (2008) Single-spike detection in vitro and in vivo with a genetic Ca²⁺ sensor. *Nat Methods* 5(9):797–804
14. Hendel T et al (2008) Fluorescence changes of genetic calcium indicators and OGB-1 correlated with neural activity and calcium in vivo and in vitro. *J Neurosci* 28(29):7399–7411
15. Neher E (1995) The use of fura-2 for estimating Ca buffers and Ca fluxes. *Neuropharmacology* 34(11):1423–1442
16. Helmchen F, Imoto K, Sakmann B (1996) Ca²⁺ buffering and action potential-evoked Ca²⁺ signaling in dendrites of pyramidal neurons. *Biophys J* 70(2):1069–1081
17. Berridge MJ, Bootman MD, Roderick HL (2003) Calcium signalling: dynamics, homeostasis and remodelling. *Nat Rev Mol Cell Biol* 4(7):517–529
18. Verkhratsky A (2005) Physiology and pathophysiology of the calcium store in the endoplasmic reticulum of neurons. *Physiol Rev* 85(1):201–279
19. Rizzuto R, Pozzan T (2006) Microdomains of intracellular Ca²⁺: molecular determinants and functional consequences. *Physiol Rev* 86(1):369–408
20. Dumont RA et al (2001) Plasma membrane Ca²⁺-ATPase isoform 2a is the PMCA of hair bundles. *J Neurosci* 21(14):5066–5078
21. Goldbeter A, Dupont G, Berridge MJ (1990) Minimal model for signal-induced Ca²⁺ oscillations and for their frequency encoding through protein phosphorylation. *Proc Natl Acad Sci USA* 87(4):1461–1465
22. Lumpkin EA, Hudspeth AJ (1998) Regulation of free Ca²⁺ concentration in hair-cell stereocilia. *J Neurosci* 18(16):6300–6318
23. Crank J (1975) *The mathematics of diffusion*, 2nd edn. Oxford University Press, London, p 424
24. Canepari M, Mammano F (1999) Imaging neuronal calcium fluorescence at high spatiotemporal resolution. *J Neurosci Methods* 87(1):1–11
25. Roberts WM (1994) Localization of calcium signals by a mobile calcium buffer in frog saccular hair cells. *J Neurosci* 14(5 Pt 2):3246–3262

26. Klingauf J, Neher E (1997) Modeling buffered Ca^{2+} diffusion near the membrane: implications for secretion in neuroendocrine cells. *Biophys J* 72(2 Pt 1):674–690
27. Nowycky MC, Pinter MJ (1993) Time courses of calcium and calcium-bound buffers following calcium influx in a model cell. *Biophys J* 64(1):77–91
28. Riley MR et al (1995) Monte Carlo simulation of diffusion and reaction in two-dimensional cell structures. *Biophys J* 68(5):1716–1726
29. Saxton MJ (1994) Anomalous diffusion due to obstacles: a Monte Carlo study. *Biophys J* 66(2 Pt 1):394–401
30. Saxton MJ (1996) Anomalous diffusion due to binding: a Monte Carlo study. *Biophys J* 70(3):1250–1262
31. Bartol TM Jr et al (1991) Monte Carlo simulation of miniature endplate current generation in the vertebrate neuromuscular junction. *Biophys J* 59(6):1290–1307
32. Kruk PJ, Korn H, Faber DS (1997) The effects of geometrical parameters on synaptic transmission: a Monte Carlo simulation study. *Biophys J* 73(6):2874–2890
33. Olveczky BP, Verkman AS (1998) Monte Carlo analysis of obstructed diffusion in three dimensions: application to molecular diffusion in organelles. *Biophys J* 74(5):2722–2730
34. Stibitz GR (1969) Calculating diffusion in biological systems by random walks with special reference to gases diffusion in the lung. *Respir Physiol* 7(2):230–262
35. Gil A et al (2000) Monte carlo simulation of 3-D buffered Ca^{2+} diffusion in neuroendocrine cells. *Biophys J* 78(1):13–33
36. Bennett MR, Farnell L, Gibson WG (2000) The probability of quantal secretion near a single calcium channel of an active zone. *Biophys J* 78(5):2201–2221
37. Segura J, Gil A, Soria B (2000) Modeling study of exocytosis in neuroendocrine cells: influence of the geometrical parameters. *Biophys J* 79(4):1771–1786
38. Coggan JS et al (2005) Evidence for ectopic neurotransmission at a neuronal synapse. *Science* 309(5733):446–451
39. He L et al (2006) Two modes of fusion pore opening revealed by cell-attached recordings at a synapse. *Nature* 444(7115):102–105
40. Stern MD, Cheng H (2004) Putting out the fire: what terminates calcium-induced calcium release in cardiac muscle? *Cell Calcium* 35(6):591–601
41. Maravall M et al (2000) Estimating intracellular calcium concentrations and buffering without wavelength ratioing. *Biophys J* 78(5):2655–2667
42. Woodruff ML et al (2002) Measurement of cytoplasmic calcium concentration in the rods of wild-type and transducin knock-out mice. *J Physiol* 542(Pt 3):843–854
43. Hiraoka Y, Sedat JW, Agard DA (1990) Determination of three-dimensional imaging properties of a light microscope system. Partial confocal behavior in epifluorescence microscopy. *Biophys J* 57(2):325–333
44. Poenie M (2006) Fluorescent calcium indicators based on BAPTA. In: Putney JW Jr (ed) *Calcium signaling*. CRC Taylor & Francis, Boca Raton, FL, p 1–50.
45. Beltramello M et al (2005) Impaired permeability to $\text{Ins}(1, 4, 5)\text{P}_3$ in a mutant connexin underlies recessive hereditary deafness. *Nat Cell Biol* 7(1):63–69
46. Spiden SL et al (2008) The novel mouse mutation Oblivion inactivates the PMCA2 pump and causes progressive hearing loss. *PLoS Genet* 4(10):e1000238
47. Lelli A et al (2003) Presynaptic calcium stores modulate afferent release in vestibular hair cells. *J Neurosci* 23(17):6894–6903